Upper atmosphere differences between northern and southern high latitudes: The role of magnetic field asymmetry

Matthias Förster[1] and Ingrid Cnossen[2,3]

[1]   The nondipolar portions of the Earth's main magnetic field constitute substantial differences between the two hemispheres. Beside the magnetic flux densities and patterns being different in the Northern Hemisphere (NH) and Southern Hemisphere (SH), also the offset between the invariant magnetic and the geographic poles is larger in the SH than in the NH. We investigated the effects of this magnetic field asymmetry on the high-latitude thermosphere and ionosphere using global numerical simulations and compared our results with recent observations. While the effects on the high-latitude plasma convection are small, the consequences for the neutral wind circulation are substantial. The cross-polar neutral wind and ion drift velocities are generally larger in the NH than the SH, and the hemispheric difference shows a semidiurnal variation. The neutral wind vorticity is likewise larger in the NH than in the SH, with the difference probably becoming larger for higher solar activity. In contrast, the spatial variance of the neutral wind is considerably larger in the SH polar region, with the hemispheric difference showing a strong semidiurnal variation. Its phase is similar to the phase of the semidiurnal variation of the hemispheric magnitude differences. Hemispheric differences in ion drift and neutral wind magnitude are most likely caused partly by the larger magnetic flux densities in the near-polar regions of the SH and partly by the larger offset between the invariant and geographic pole in the SH, while differences in spatial variance are probably just caused by the latter. We conclude that the asymmetry of the magnetic field, both in strength and in orientation, establishes substantial hemispheric differences in the neutral wind and plasma drift in the high-latitude upper atmosphere, which can help to explain observed hemispheric differences found with the Cluster/Electron Drift Instrument (EDI) and the Challenging Minisatellite Payload (CHAMP).

1.   Introduction

[2]   The Earth's main magnetic field, generated by internal dynamo processes in the outer fluid core, is mostly dipolar at the Earth's surface and above. However, about 10% of the magnetic field is made up of nondipolar contributions, which result in asymmetries between the Northern Hemisphere (NH) and Southern Hemisphere (SH). A persistent decrease of the dipole moment at least since the beginning of the systematic, full vector field measurements around 180 years ago and the recent strong acceleration of the north magnetic pole motion [*Olsen and Mandea*, 2007] give reason to reflect on geomagnetic pole excursions or even field

reversals within relatively short times [e.g., *Constable and Korte*, 2006]. Changes of the north and south magnetic poles are independent and not directly correlated to variations of the Earth's dipolar axis [*Korte and Mandea*, 2008]. In this study, we will be focusing on the present-day magnetic field asymmetry at high latitudes and at an altitude of approximately 400 km.

[3]   The current near-polar geomagnetic flux density $|\vec{B}|$ at 400 km altitude according to the International Geomagnetic Reference Field (IGRF) [*Finlay et al.*, 2010] is shown in Figure 1 for both hemispheres. The NH polar region is characterized by two foci of flux density in the Canadian and the Siberian sectors, respectively, while there is one major focus only in the SH. Actual average values of the IGRF $|\vec{B}|$ within a circumpolar region inside 80° magnetic latitude at 400 km altitude amount to 46,261 nT for the NH versus 51,332 nT for the SH. The (symmetric) geomagnetic dipole positions are indicated with dark blue asterisks in Figure 1, while the magnetic (dip) poles (vertical $\vec{B}$ inclination points) are shown as light blue crosses. The geophysically effective invariant magnetic pole positions, where the invariant magnetic latitude is equal to 90° [cf., e.g., *Emmert et al.*, 2010],

[1]GFZ German Research Centre for Geosciences, Potsdam, Germany.
[2]British Antarctic Survey, Cambridge, UK.
[3]High Altitude Observatory, National Center for Atmospheric Research, Boulder, Colorado, USA.

Corresponding author: M. Förster, GFZ German Research Centre for Geosciences, Helmholtz Centre Potsdam, Telegrafenberg, 14473 Potsdam, Germany. (mfo@gfz-potsdam.de)
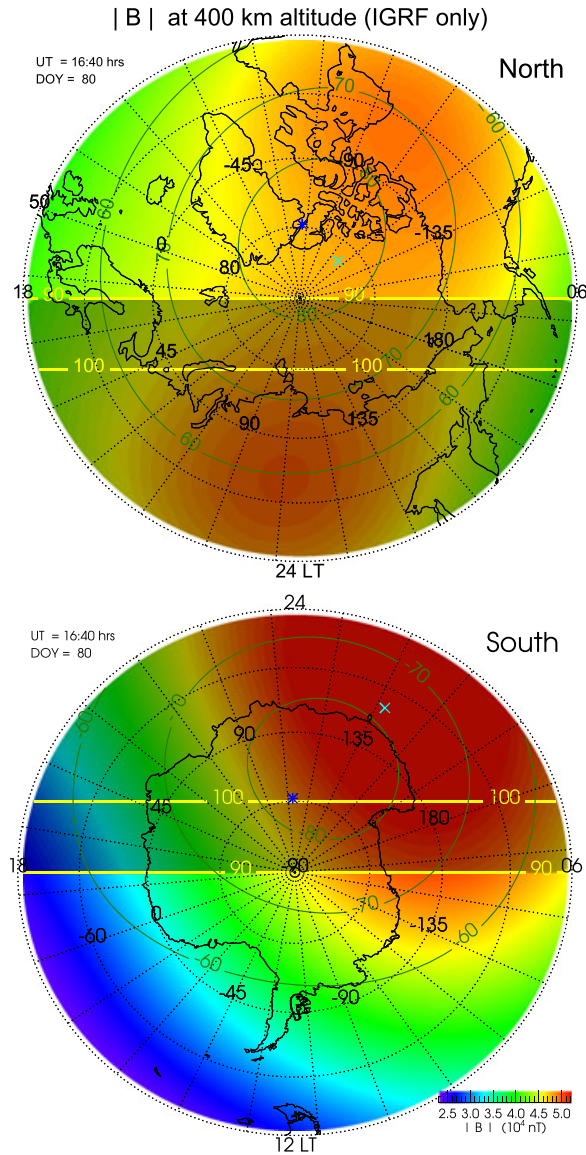
Figure 1. Geomagnetic IGRF flux density $|\vec{B}|$ at 400 km altitude for the present era over the (top) northern and (bottom) southern polar regions, shown as color-coded contour plots with the same scale (bottom right). The dipole axis orientation (geomagnetic poles) are indicated with dark blue asterisks and the magnetic poles (or dip pole positions) with light blue crosses. The green isolines show geomagnetic parallels of altitude-adjusted corrected geomagnetic coordinates (AACGM). The yellow solar zenith angle lines and the shading illustrate the solar illumination during equinox at 16:40 UT.

can be seen as the focal points of the corrected geomagnetic parallels, drawn as green lines. The invariant poles are offset from the rotation axis by $\sim$8° and $\sim$16° in the NH and SH, respectively.

[4] The Earth's magnetic field plays an important role in the near-Earth space environment and the upper atmosphere. Through its extended magnetosphere, it acts as a shield from highly energetic cosmic and solar particle fluxes while at the same time determining where any particles that do get through enter the Earth's upper atmosphere. The

magnetosphere also interacts with the interplanetary magnetic field (IMF) carried by the solar wind, and this interaction drives high-latitude electric fields and plasma convection in the upper atmosphere, which also leads to Joule heating of the thermosphere.

[5] Modeling studies by *Cnossen et al.* [2011, 2012a, 2012b] have shown that both the strength and the orientation of the magnetic field can affect the coupling between the solar wind and magnetosphere and thereby influence the ionosphere and thermosphere. There are also additional influences of the magnetic field within the upper atmosphere itself, via its effect on ionospheric conductivity and plasma transport processes [*Cnossen and Richmond*, 2012]. The modeling studies just mentioned all focused on dipolar changes in the magnetic field, which could have occurred at different stages of (geological) history or might occur in the future. Only hemispherically symmetric changes were considered. However, one might expect that the north-south asymmetry present in the current magnetic field could lead to differences in the upper atmosphere between the two hemispheres in similar ways.

[6] Indeed, several studies have found observational evidence for hemispheric differences, which could potentially be linked to north-south differences in the magnetic field. For instance, analyzing thermal ion drift measurements of the Defense Meteorological Satellite Program (DMSP), *Papitashvili and Rich* [2002] showed interhemispheric asymmetry features with their empirical ionospheric convection model. The average hemispheric cross-polar cap potentials (CPCP) were found to be asymmetric even during equinox intervals with a NH to SH ratio of $\sim$0.9. They suspect that hemispheric asymmetries in the geomagnetic field and magnetospheric sources in a geographic reference frame determine this imbalance.

[7] Averaged thermospheric neutral wind measurements from Dynamic Explorer 2 (DE 2) satellite in the early 1980s [*Hays et al.*, 1984] were analyzed in detail by *Thayer and Killeen* [1993]. They combined the observations with theoretical model calculations to investigate the high-latitude thermospheric neutral wind field for December solstice conditions during high solar activity in 1981–1982 and 1982–1983. They decomposed the polar wind field with their kinematic analysis into divergent (irrotational) and nondivergent (rotational) components and calculated corresponding potential and stream functions for various levels of geomagnetic activity. The latter is shown to be driven primarily by the ion-drag and Coriolis forces, while the irrotational component is representative of the solar-driven cross-polar neutral wind, directed primarily along the 14-02 MLT plane. *Thayer and Killeen* [1993] noted generally larger polar cap wind magnitudes in the SH compared to the NH for their study interval.

[8] A recent study of *A et al.* [2012] investigated density enhancements in the polar regions of both hemispheres during 102 geomagnetic storms between May 2001 and December 2007, based on accelerometer data of the CHAllenging Minisatellite Payload (CHAMP) satellite [*Reigber et al.*, 2002]. They found out that the density enhancements in the southern polar region were on average much larger than in the northern polar region. The comparisons of density versus *Dst* and *Ap* indices indicated a strong linear dependence with the slopes of the fitted lines in the SH being 50% greater

than those in the NH. They suspected that this effect might possibly be attributed to the hemispherically nonsymmetric geomagnetic field [*A et al.*, 2012].

[9] *Förster et al.* [2008, 2011] studied thermospheric wind and vorticity patterns at high latitudes based on CHAMP data. The thermospheric mass density and neutral thermospheric wind were measured with a newly developed accelerometer onboard the CHAMP satellite which was orbiting the Earth at a circular, near-polar orbit at ~400 km altitude during the last decennium. Data were obtained from 2001 to 2010. This huge data set was recently reanalyzed and recalibrated by the European Space Agency [*Doornbos et al.*, 2010] and provides a comprehensive base for statistical studies of thermospheric behavior in response to external drivers. *Förster et al.* [2008, 2011] analyzed averaged patterns of the high-latitude neutral wind circulation and their dependence on solar wind parameters, in particular the IMF orientation. They found observational evidence for hemispheric differences in thermospheric wind and vorticity patterns at high magnetic latitudes and suggested that these differences might be explained by the asymmetry of the magnetic field. It is the purpose of this study to test that idea further using simulations with the Coupled Magnetosphere-Ionosphere-Thermosphere (CMIT) model with hemispherically symmetric and asymmetric magnetic field configurations.

[10] This paper is organized as follows. In section 2 we briefly describe the CMIT model and the setup of our simulations, followed by a description of the data analysis performed. In section 3 the results are presented, starting with a general view of the hemispheric differences in high-latitude neutral wind and plasma drift. We also analyze the dependence of the hemispheric differences on UT and IMF orientation. This is done for the magnitudes of high-latitude neutral winds and ion drifts in section 3.1 and for their cross-polar directions in section 3.2. In section 3.3 we show results for the neutral wind vorticity and divergence. This is followed by a discussion of the results in section 4 and conclusions in section 5.

2. Methodology

2.1. Model Description

[11] In the present study, we use the Coupled Magnetosphere-Ionosphere-Thermosphere (CMIT) model [*Wiltberger et al.*, 2004; *Wang et al.*, 2004, 2008]. CMIT couples the Lyon-Fedder-Mobarry (LFM) magnetospheric MHD code [*Lyon et al.*, 2004] with the Thermosphere-Ionosphere-Electrodynamics General Circulation Model (TIE-GCM) [*Roble et al.*, 1988; *Richmond et al.*, 1992] through the Magnetosphere-Ionosphere coupler/solver (MIX) module [*Merkin and Lyon*, 2010].

[12] The LFM component of the model solves the ideal magnetohydrodynamic (MHD) equations to simulate the interaction between the solar wind and the magnetosphere and calculates the full MHD state vector (plasma density, pressure, velocity, and magnetic field). It requires the solar wind MHD state vector on its outer boundary as input and the ionospheric conductance on its inner boundary. The latter is passed in from the TIE-GCM part of the code through the MIX coupler module. An empirical parameterization described by *Wiltberger et al.* [2009] is used to calculate the energy flux of precipitating electrons into the upper atmosphere.

[13] The TIE-GCM is a time-dependent, three-dimensional model that solves the fully coupled, nonlinear, hydrodynamic, thermodynamic, and continuity equations of the thermospheric neutral gas self-consistently with the ion continuity equations. At high latitudes it requires the auroral particle precipitation and electric field imposed from the magnetosphere, which in CMIT it receives from the LFM component of the code via the MIX coupler module. The solar activity level is specified through an $F_{10.7}$ value. At the lower boundary (~97 km altitude), tidal forcing can be provided by the Global Scale Wave Model (GSWM). In our simulations we used the GSWM migrating diurnal and semidiurnal tides of *Hagan and Forbes* [2002, 2003]. While the TIE-GCM can be run at different spatial resolutions, we used here a 5°×5° global grid. The CHAMP data analysis is based on binned data with a spacing of 2° in magnetic latitude and approximately equal spacing in magnetic longitudinal direction. There is therefore a factor of ~2 difference in the grid resolution, but we expect that any effects of this difference are relatively small and are sufficiently unimportant for our results that they can be ignored.

[14] To test the influence of the asymmetry in the Earth's magnetic field on hemispheric differences in the upper atmosphere, we used two different simulation setups. In the first simulation we used a centered dipolar magnetic field with a dipole moment of $7.7 \times 10^{22} Am^2$ and the NH geomagnetic pole located at 80°N and 70°W. This is close to the best fitting dipole of the present-day magnetic field. In the second simulation we used a more realistic magnetic field, specified by the IGRF [*Finlay et al.*, 2010]. By comparing the hemispheric differences for both cases, we can infer how much of those differences are associated with the hemispheric asymmetry of the Earth's magnetic field.

2.2. Simulation Interval

[15] We selected a simulation interval near equinox to avoid hemispheric differences arising from different seasons, which would further complicate our analysis. The interval used was 20 March to 8 April or day of year (DoY) 80–99 in 2008, during a period of low solar activity and moderate geomagnetic activity. The 81 day average (three Bartels' rotations) solar radio flux index $\overline{F_{10.7}}$ is 71, and the daily $F_{10.7}$ varied between 68 and 88 due to a M2-class solar flare on 25 March 2008. The planetary magnetic Kp index does not exceed 5_O, but the interval includes two moderate geomagnetic storm periods with sudden storm commencements (ssc) on 26 March (DoY 86) at 09:36 UT and on 4 April (DoY 95) at 15:03 UT and 15:10 UT. The AE index during these two storms attains peak values of ~1500 nT; the Dst values vary between +25 nT and –43 nT. Our study interval coincides with the first Whole Heliosphere Interval (WHI 1: Carrington Rotation 2068), which aimed at dedicated studies of the extremely low solar activity during the recent extended solar-cycle minimum. The WHI 1 illustrated the effects of fast solar wind streams on the Earth in an otherwise quiet heliosphere [*Bisi et al.*, 2011]. This interval was also part of the model study of *Wiltberger et al.* [2012], who examined the geospace effects of corotating interaction regions (CIRs), preceded by high-speed streams (HSS) of solar wind. They analyzed the response of the
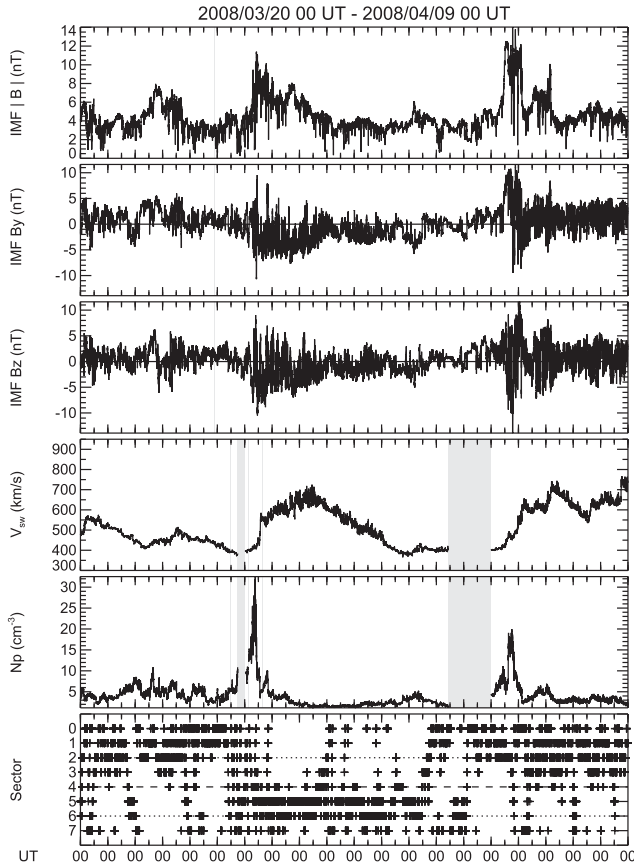
Figure 2. Solar wind and IMF conditions during the 20 day model interval of 20 March to 8 April 2008 (DoY 80–99), obtained from ACE observations in the solar wind upstream of Earth and time shifted to the magnetopause position. The grey-shaded areas indicate periods of missing data. (top to bottom) Shown are the IMF magnitude, the IMF y and z components in GSM coordinates, the solar wind velocity, the solar wind plasma density, and the corresponding sector of the IMF orientation in the GSM y-z plane (see text).

thermospheric density during these intervals using the CMIT model as well and compared the results with CHAMP satellite observations.

[16] Figure 2 shows the solar wind and IMF conditions during the modeled interval near spring equinox from 20 March at 00 UT to 8 April 2008 at 24 UT. The IMF values obtained by the Advanced Composition Explorer (ACE) spacecraft at the Earth-Sun L1 libration point upstream of Earth are time shifted to the frontside magnetopause, using the phase front propagation technique [*Weimer et al.*, 2003] in the modification according to *Haaland et al.* [2006]. From top to bottom, Figure 2 depicts the IMF magnitude, the two important components B_y^{IMF} and B_z^{IMF}, the solar wind speed and plasma density, and finally the so-called "sector" orientation of the IMF. It represents a classification into eight separate, 45° wide cones (sectors) of the IMF vector direction, projected into the y-z plane of the Geocentric Solar Magnetospheric (GSM) system. Sector 0 stands for ±22.5° around purely northward orientation or 0° IMF clock angle. Both sector number and IMF clock angle are then counted toward the y axis in the GSM y-z plane, clockwise when

looking from the Sun. Sector 1 means therefore an IMF orientation of (positive) $B_y^{\mathrm{IMF}}+$ and $B_z^{\mathrm{IMF}}+$, sector 2 denotes straight duskward $B_y^{\mathrm{IMF}}+$ values, and so forth. The strongest interaction between the solar wind IMF and the Earth's magnetosphere, with the most intense reconnection, is expected for southward IMF, i.e., (negative) $B_z^{\mathrm{IMF}}-$ (sector 4). The most likely IMF orientations are in the ecliptic plane, so that maxima of occurrence rates are usually noticed around sectors 2 ($B_y^{\mathrm{IMF}}+$) and 6 ($B_y^{\mathrm{IMF}}-$) [cf. *Haaland et al.*, 2007, Figure 1]. During the first 6 days of our model interval, as shown in Figure 2, $B_y^{\mathrm{IMF}}+$ conditions predominate, followed by 6–7 days with $B_y^{\mathrm{IMF}}-$, including a high-speed solar wind period from DoY ∼86–89, and predominant $B_y^{\mathrm{IMF}}+$ values again during the rest of the model interval, partly with high-speed solar wind episodes as well.

[17] Both the simulation with the dipolar magnetic field and the simulation with the IGRF magnetic field were run continuously over the 20 day period with the same external drivers and boundary conditions, according to the observed natural variations of the solar wind, IMF, and solar radiation parameters.

2.3. Data Analysis Method

[18] The guiding idea of this study is to analyze statistically the model simulation results of neutral thermospheric wind and ionospheric plasma drift at high latitudes in the same manner as it was done with the observational data of the CHAMP accelerometer wind estimations [*Förster et al.*, 2008; *Förster et al.*, 2011] and the Cluster/Electron Drift Instrument (EDI) drift measurements [*Haaland et al.*, 2007; *Förster et al.*, 2007]. We compare the two different model simulations with each other and consider their principal behavior in the context of observational findings.

[19] We analyzed the horizontal neutral thermospheric wind and F region plasma drift, which were extracted globally from the TIE-GCM geographic grid with a 6 min cadence at pressure level 25, corresponding to an altitude of about 400 km. A snapshot of the neutral wind circulation at high geographic latitudes of both hemispheres in the form of color-coded wind vector plots is presented in Figure 3 as an example (color-coded wind arrows; right-hand scale). This snapshot was taken at DoY 87 (March 27) at 16:36 UT, during a moderate disturbance period with $B_z^{\mathrm{IMF}}-$ and $B_y^{\mathrm{IMF}}-$ conditions (sector 5). The UT time is close to the maximum tilt of the northern geomagnetic pole toward the Sun (the southern pole position is correspondingly near its maximum tilt away from the Sun). The largest neutral wind speeds globally are seen at these high latitudes $|\phi| > 60°$, as expected, and a hemispheric difference is obvious with larger speeds over the northern polar region compared with the southern polar region.

[20] Figure 3 also shows the model electric potential distribution as background color with its scale on the left-hand side. The invariant magnetic pole position is indicated with a magenta triangle sign. The streamlines of the electric potential distribution correspond to the ionospheric plasma drift motion. The CPCP, indicated in the left upper corner, is a measure of the energy input by the external forces, which drive a global-scale current system, powered by reconnection processes at the frontside magnetopause and in the tail region. The large round duskside circulation cell in the SH
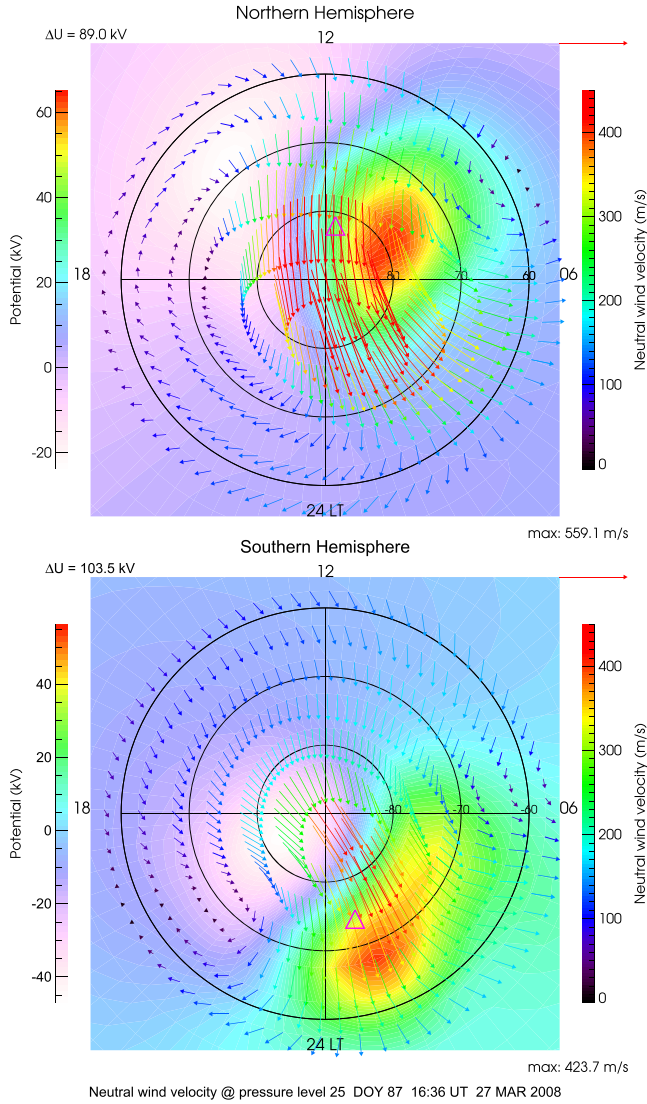
Figure 3. Upper atmosphere neutral wind pattern at high geographic latitudes and model pressure level 25 (≈ 400 km altitude) for both (top) NH and (bottom) SH. The neutral wind vectors are shown as scaled and color-coded arrows according to the right-side color bars. The maximum wind speed is indicated on the right bottom of each panel. The background color according to the left-side color bars shows additionally the model electric potential distribution with the cross-polar cap potential value at this time in the left upper corner. The magenta triangle indicates the position of the invariant magnetic poles. As shown in Figure 2, this time is characterized by $B_y^{\mathrm{IMF}}-$ and $B_z^{\mathrm{IMF}}-$ conditions ("sector 5").

plasma drift at F layer height for both hemispheres have been deduced from this large data set and analyzed with respect to various solar wind, geomagnetic, and particularly IMF conditions, as described in the companion papers of *Haaland et al.* [2007] and *Förster et al.* [2007]. Their dependence on the IMF strength and orientation was also modeled analytically by *Förster et al.* [2009].

[22] The CMIT model results have to be transformed first from geographic coordinates into geomagnetic coordinates, because the thermospheric behavior at high latitudes is better ordered with respect to geomagnetic rather than geographic coordinates, which has been well known for a long time [e.g., *Hays et al.*, 1984; *Killeen et al.*, 1995]. This is even much more obvious for the plasma motion. For the first model run with the dipole magnetic field symmetry, the transformation is simply from geographic coordinates into centered-dipole magnetic coordinates (MAG). For the second model simulation using the IGRF, the efforts are more complex, as one has to use one of the various approaches to corrected geomagnetic coordinates [*Hultqvist*, 1958]. Possible options would be to use the Modified Apex Coordinates or quasi-dipole (QD) coordinates [*Richmond*, 1995]. However, in this study, we use Altitude Adjusted Corrected Geomagnetic Coordinates (AACGM) [*Baker and Wing*, 1989], analogous to the data analyses with the CHAMP and Cluster/EDI data mentioned above.

[23] First we selected all data within a spatially confined region in the central polar cap to calculate average values and higher-order moments for the cross-polar drift and neutral wind velocities, as it was done in the statistical study of, e.g., *Förster et al.* [2007] with Cluster/EDI data. We selected all circumpolar data at magnetic latitudes $|\phi_m| > 80°$ and calculated the average magnitude and direction. The statistical moments were calculated as weighted averages according to the area of the model's bin sizes.

[24] We then analyzed the model simulation data similarly to the observational data, deriving statistical properties by sorting them with respect to IMF orientation (sectors) and UT dependence. We also checked the IMF stability by applying the so-called "bias-vector" technique as explained in *Haaland et al.* [2007, Figure 3]. The magnitude of a bias vector over a certain period of IMF vectors gives a measure of their average variability. In our study, the averaging interval comprised 30 min, starting 20 min before and ending 10 min after the actual time of measurement. The procedure of sorting for specified IMF directions (clock angle sectors) and the optional bias-value filtering of solar wind data for stable IMF conditions has been described in the papers of *Haaland et al.* [2007] and *Förster et al.* [2007]. Here, we use the same methodology with the same bias value (≥ 0.96) threshold as for the Cluster/EDI plasma convection analyses and previous high-latitude neutral wind studies [*Förster et al.*, 2008, 2011].

[25] In contrast to satellite data, which require a statistical treatment to deduce physical regularities and dependences due to their nature of irregularly distributed "one-point measurements," the model data have the advantage that they can be sampled in principle with any resolution and continuously in space and time. But the simulation results are, on the other hand, "predetermined" in the sense that the model is based on first-principle physical laws, the results of which are, in principle, known. However, due to the complexity of

pattern (bottom) and the more crescent-shaped one on the dawn side are typical for sector 5 (negative $B_y^{\mathrm{IMF}}-/B_z^{\mathrm{IMF}}-$) potential patterns, while the opposite is true for the NH (top) [e.g., *Ruohoniemi and Greenwald*, 2005].

[21] The model output level (pressure level 25, ≈ 400 km) coincides approximately with the altitude of mapping the Electron Drift Instrument (EDI) electric field measurements [*Paschmann et al.*, 1997, 2001] obtained onboard the Cluster satellite fleet [*Escoubet et al.*, 1997] over the last decennium since February 2001. Statistical patterns of high-latitude
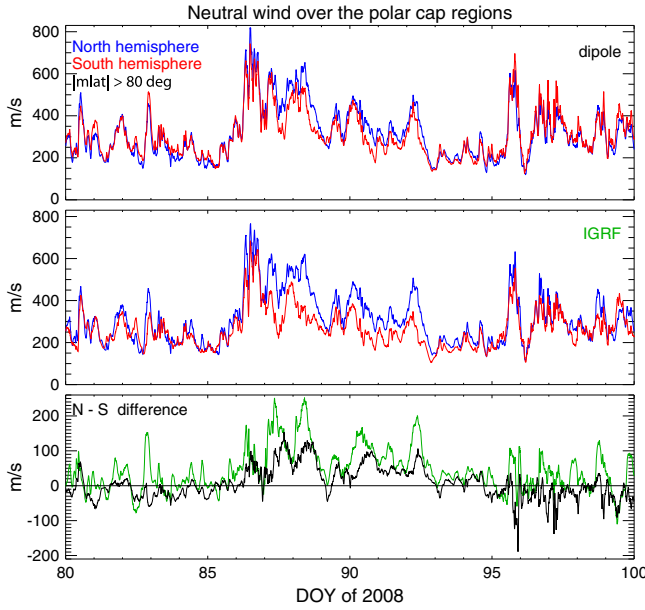
Figure 4. Model neutral wind speeds of the high-latitude upper atmosphere at pressure level 25 (about 400 km), averaged over the central polar cap regions within magnetic latitudes $|\phi_m| > 80°$, during the full 20 day period for both the NH (blue lines) and the SH (red). (top) The model case of a symmetric geomagnetic dipole. (middle) The results for a more realistic magnetic field configuration, assuming the IGRF model. (bottom) Comparison of the north-south hemispheric differences, shown in Figure 4 (top and middle), i.e., for both the dipole case (black) and the IGRF case (green).

the model and its internal interdependences, the results may still be unpredictable and even chaotic in nature.

3. Model Results

3.1. Magnitude of Neutral Wind and Plasma Drift

[26] Figures 4 and 5 show time series of the high-latitude average cross-polar neutral wind and ionospheric plasma drift, respectively, for the whole 20 day simulation interval, with blue and red colors distinguishing between the NH and SH. Figures 4 (top and middle) and 5 (top and middle) present the model simulation runs with the dipole and IGRF simulation. This scheme of presentation will be kept for all subsequent line plots in the remainder of this paper. Figures 4 (bottom) and 5 (bottom) display here for clarity the north-south difference of the parameter values shown in Figures 4 (top and middle) and 5 (top and middle)—for a direct comparison of hemispheric differences between the dipole case (black line) and the IGRF case (green).

[27] The magnitude of both the neutral winds and drifts exhibit a clear correlation with the IMF and solar wind parameters as shown in Figure 2. This reflects the level of storm and substorm activity, which is associated with geomagnetic disturbances. The average cross-polar neutral wind speed (Figure 4) clearly reveals differences between the reactions in the NH and SH for the two different model runs. While in the dipole case both curves ("blue" and "red") more or less closely follow each other (with a few minor exceptions around DoY 87–88), there are larger differences for the

IGRF case. This is in particular the case during periods of $B_y^{IMF}-$ in the middle third of the interval (DoY 86–92). There the NH thermospheric wind speed clearly exceeds the SH one, which is even more obvious in Figure 4 (bottom) with the north-south differences.

[28] The ionospheric plasma drift speed at F region height (≈ 400 km) in Figure 5 shows strong fluctuations with maximum values up to 1600 m/s during the storm days. This temporal variability is associated with the large variability of the driving forces. Hemispheric differences in the resulting drift magnitudes can be noticed in the IGRF simulation (Figure 5, middle), but are hardly seen in the dipole case (Figure 5, top). The IGRF case shows almost continuously larger drift values in the NH (i.e., positive north-south differences, green line), with larger peaks during the storm days (DoY 86–88 and 95–97).

[29] To gain additional clues on the causes of the north-south differences, we also investigate their dependence on UT and on the IMF clock angle. We first examine the UT dependence. Figure 6 shows the diurnal variation of the neutral thermospheric wind and the ionospheric drift velocities in the top and bottom, respectively, for both model runs. Here, we sorted the high-latitude ($|\phi_m| > 80°$) averages with respect to UT into 2 h wide bins. The solid lines present the mean values of the high-latitude averages within each UT bin, while the dotted lines show their $\pm$standard deviation within each bin.

[30] In these line plots, the differences between the two model realizations are quite evident. While the hemispheric differences of the average magnitudes in the dipole case are small in the case of the neutral wind (Figure 6, top) or practically nonexistent in the case of the ion drift (Figure 6, bottom), there are differences up to about 15% for the
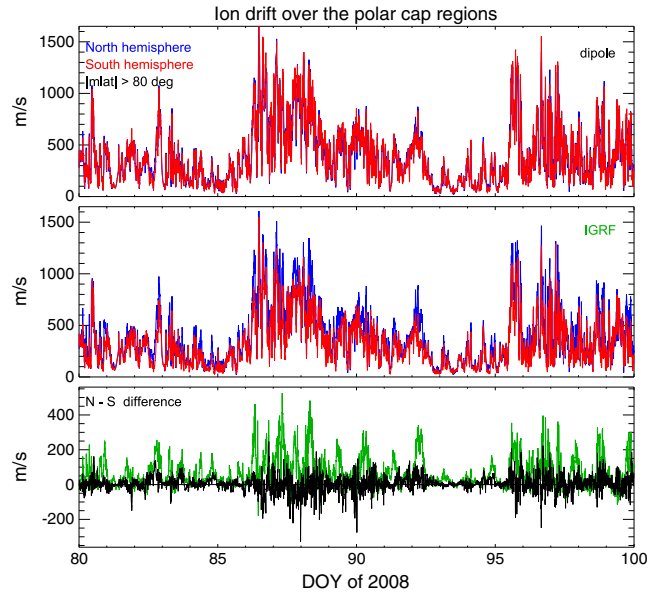

Figure 5. Similar to Figure 4 but for the model plasma drift velocity at high magnetic latitudes $|\phi_m| > 80°$ of both hemispheres for (top) the dipole and (middle) the IGRF simulation. The plasma drift magnitudes show a much larger temporal variability due to the external driving forces, mainly the reconnection processes of the solar wind IMF with the geomagnetic field.
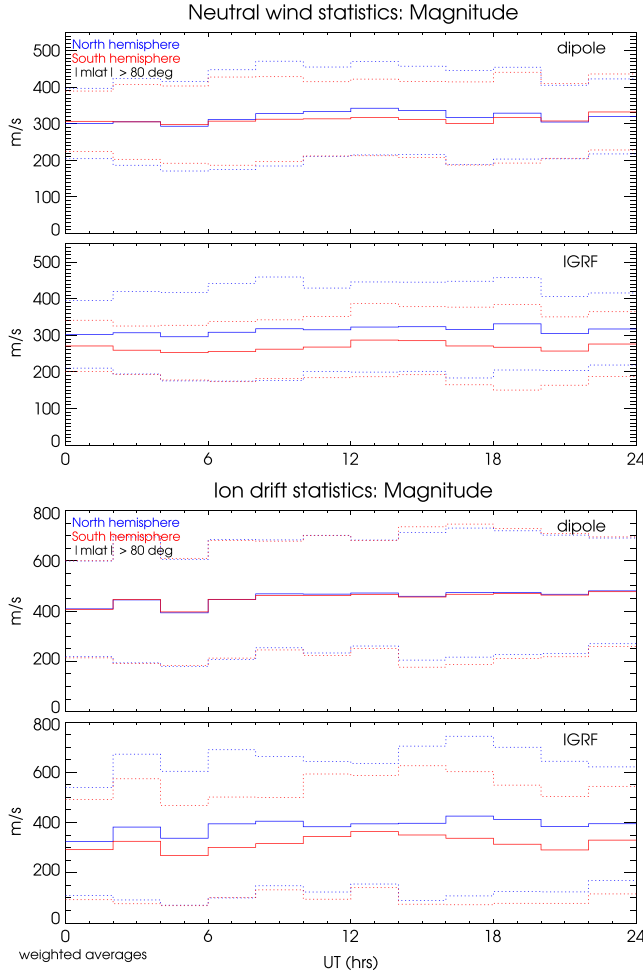
Figure 6. Diurnal variation of the (top) model neutral wind speed averages and (bottom) ionospheric plasma drift within the central polar cap regions ($|\phi_m| > 80°$) in the NH (blue) and SH (red lines) and for both the dipole and IGRF simulation. The standard deviations of the 2 h box averages are indicated by the dotted lines.

IGRF case. The NH average velocity magnitudes are larger throughout the day and show a slight semidiurnal variation with minimum north-south differences near 12 UT and 24 UT. This concerns both the neutral wind and the ion drift, but the differences are more consistent throughout the whole diurnal period for the neutral wind, while the semidiurnal variation of this difference is more clearly visible in the ion drift magnitudes with maxima in the 04–10 UT and 16–22 UT ranges.

[31] We now examine the dependence of the north-south differences on IMF clock angle. Figure 7 shows both the average neutral cross-polar wind (solid lines) and the ion drift (dashed lines) as a function of IMF clock angle orientation (sectors) for the two model simulations. The variation of both parameters with B_z^{IMF} is evident: there are clear minima for northward IMF (sector 0) and maxima for southward IMF with a preference to $B_y^{\text{IMF}}-$ (sector 5) in the averages over this modeled time interval.

[32] The ion drift averages for the two hemispheres coincide for the dipole case (Figure 7, top, dashed lines), while

they show a hemispheric difference for the IGRF case, with larger average drift magnitudes for all IMF orientations in the NH (Figure 7, bottom, dashed lines). This hemispheric difference in plasma drift speed does not depend much on the IMF sector. It amounts on average to ~75 m/s with somewhat larger values (~100 m/s) for southward IMF, in particular for sector 5. It corresponds to the average hemispheric differences in the diurnal course as shown in Figure 6, while these systematic differences were hardly seen in Figure 5 with its strong fluctuations.

[33] The neutral thermospheric wind averages of the central polar cap from both the dipole and IGRF simulation, on the other hand, reveal a B_y^{IMF} dependency, which was also found in the observational data set of CHAMP [see, e.g., *Förster et al.*, 2008, Tables 1 and 2]. This dependency is small, with opposite sign for opposite B_y^{IMF} sectors, so that it tends to average out, e.g., in the UT dependence (Figure 6). This effect might be weaker in the simulations than in the observations due to the difference in solar activity level, i.e., the very low level in 2008 for this study versus the moderate to high solar activity with some strong geomagnetic "superstorms" in 2003 that were sampled in the study of *Förster et al.* [2008]. For the IGRF simulation, the IMF clock angle dependence of the neutral wind speed is superposed by a general shift of the wind speeds toward larger values in the NH.

[34] Figure 8 shows the standard deviation (STDEV) values of the model neutral wind speeds—again for the whole simulation interval. It is calculated for each individual model time step as the deviation from the mean value, shown in Figure 4, of all grid points within the circumpolar north and south polar cap regions with $|\phi_m| > 80°$, so it provides a measure of the spatial variability within the central polar cap region. The values are weighted according to the area that is covered by each individual grid point. While there are minor
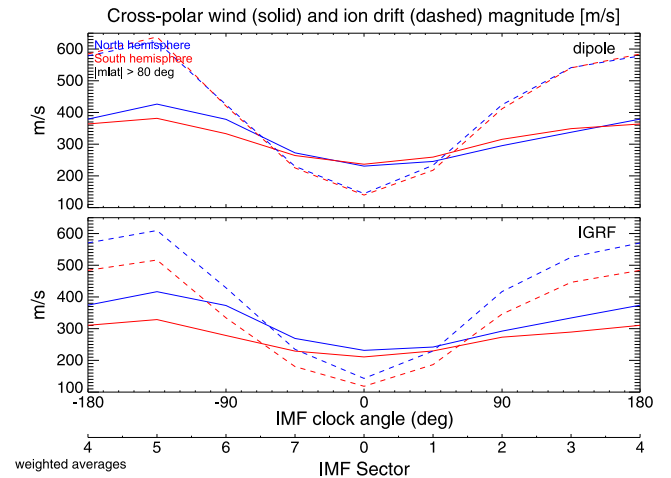

Figure 7. Dependence of the neutral wind (full lines) and ionospheric plasma drift magnitudes (dashed lines) within the central polar cap regions ($|\phi_m| > 80°$) of the NH (blue) and SH (red) on the IMF vector orientation. This IMF orientation is sorted into eight 45° wide bins ("sectors") in the GSM *y-z* plane, counted clockwise, starting with sector "0" for purely northward IMF, sector "2" for $B_y^{\text{IMF}}+$, sector "4" for southward IMF ($B_z^{\text{IMF}}-$), and sector "6" for $B_y^{\text{IMF}}-$.
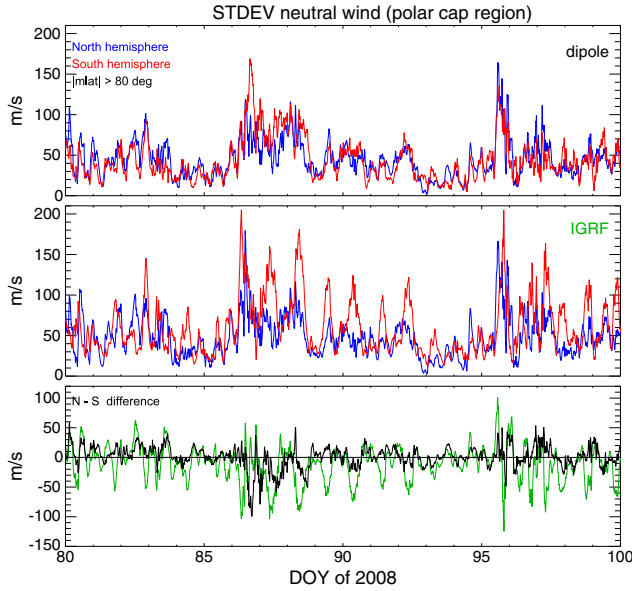
Figure 8. Model neutral wind standard deviations of wind speed averages within the central polar cap regions ($|\phi_m| > 80°$) of both hemispheres as shown in Figure 4. The blue and red lines are for the NH and SH, respectively. The two different model runs, i.e., (top) dipole geomagnetic field and (middle) IGRF. (bottom) Comparison of the north-south hemispheric differences, shown in Figure 8 (top and middle), i.e., both the dipole case (black) and the IGRF case (green).

differences between the hemispheres for the dipole simulation (Figure 8, top), except during the first major storm day (DoY 86), there are again more systematic hemispheric differences in the case of the IGRF simulation (Figure 8, middle). In contrast to the neutral wind speeds for the IGRF case, which are generally larger in the NH (as shown in Figures 6, bottom and 7, bottom), the neutral wind STDEV values of the SH mostly exceed those of the NH by up to a factor of 2 indicating greater spatial variability in the SH.

[35] Already in the time series presented in Figure 8, it can be seen that the north-south differences in the standard deviation of the neutral wind appear to have a diurnal periodicity for the IGRF case. This becomes even clearer after sorting the data with respect to UT, as shown in Figure 9. While the average standard deviations are quite constant over the day in the dipole simulation, there are distinctly different variations in the opposite hemispheres for the IGRF simulation. There is a quasi-semidiurnal variation that is much more pronounced in the SH than in the NH, and also the phase is different in the two hemispheres. In the SH the main maximum occurs in the 08–10 UT bin, with a secondary maximum at 18–20 UT, while the maxima in the NH are phase-shifted by about 4 h to later times and are less well pronounced. The NH and SH standard deviations become approximately equal during the periods of maximum tilt deflection toward and away from the Sun near 04:40 UT and 16:40 UT (for the dipolar axis).

3.2. Neutral Wind and Plasma Drift Direction

[36] For the neutral wind and plasma drift directions, we will go straight to the results after binning with respect to
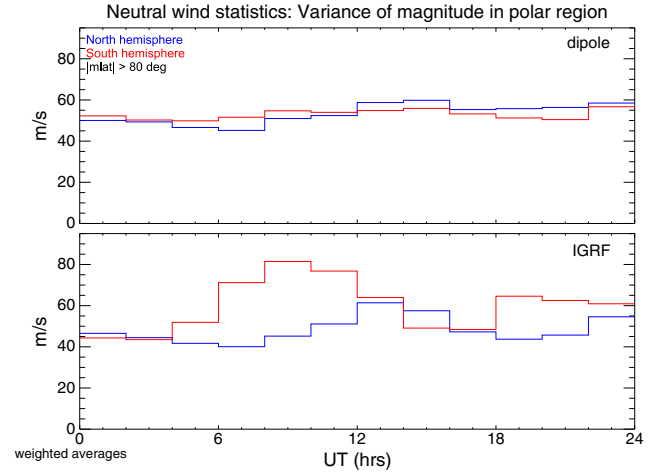

Figure 9. Diurnal variation of the standard deviations for the model neutral wind speed averages within the central polar cap regions ($|\phi_m| > 80°$) as shown in Figure 6. The blue and red lines stand for the NH and SH variations, respectively. (top) The model run with the dipole geomagnetic field assumption and (bottom) the corresponding model run with the IGRF.

UT and IMF clock angle sector was done, starting again with the UT dependence of the north-south differences. Figure 10 shows the diurnal variation of the average cross-polar neutral wind direction over the polar caps (solid lines), again together with the average scatter (±standard deviation) within the 2 h bins (dotted lines). The wind vector direction is counted clockwise from the noon meridian, when looking the same way at both polar regions, i.e., from a point above the NH, as if looking through a transparent Earth to see the southern polar region. A strictly straight antisolar motion along the noon-midnight meridian corresponds to a 180° direction.
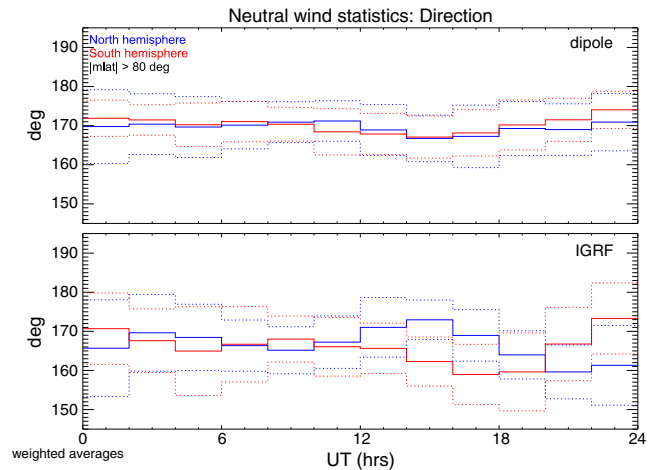

Figure 10. Diurnal variation of model neutral wind averages within the central polar cap regions ($|\phi_m| > 80°$) as shown in Figure 6 but here with respect to the cross-polar neutral wind direction, counted clockwise (CW) from the noon meridian when viewed from above the North Pole. The dotted lines show the standard deviation of the 2 h boxes' averages.
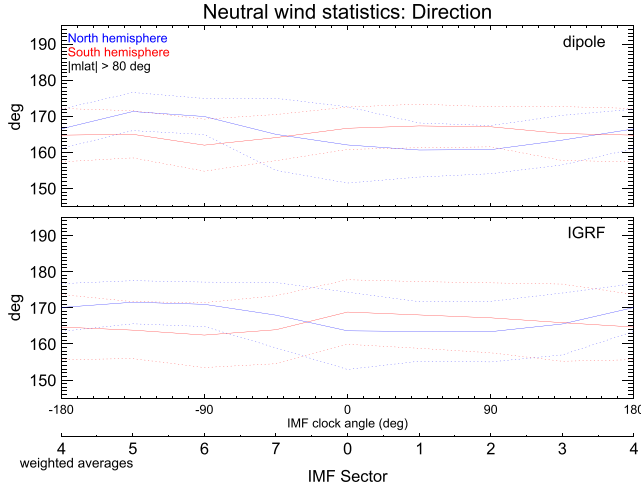
Figure 11. Model neutral wind direction averages within the central polar cap regions ($|\phi_m| > 80°$) drawn versus the IMF orientation (sectors). The blue and red solid lines show the average direction for the NH and SH, respectively, counted CW from the noon meridian from above the North Pole for both hemispheres like in Figure 10. The dotted lines indicate the ranges of $\pm 1\sigma$ standard deviations within each sector's bin.

[37] While there are only small hemispheric differences for the dipole case, some differences are evident between the NH and the SH for the IGRF case, mainly during the second half of the day, with maximum differences of up to about 10° around 16 UT and just prior to 00 UT. Around 16 UT, the neutral wind over the southern central polar cap region points more dawnward than the neutral wind over the northern polar cap, and vice versa during the later period. The average directions of cross-polar ion drift motion (not shown here) reveal similar systematic north-south differences over the day with maximum differences up to 35°, but the mean overall direction is closer in line with the noon-midnight meridian ($\sim180°$).

[38] Figure 11 presents the average neutral cross-polar wind direction as a function of the IMF clock angle (sectors). The direction of the motions is counted again clockwise from the noon meridian as in Figure 10 above when viewed from above the North Pole. The average cross-polar neutral wind direction shows systematic variations with the IMF clock angle, apparently in antiphase between the hemispheres. These systematic variations are quite similar for the two model runs, with a more dawnward orientation of the neutral wind (by up to $\sim10°$) during conditions with $B_y^{IMF}-$ (sectors 4–7) in the SH, and more dawnward oriented neutral winds (by $\sim10°$ in case of the dipole simulation and by $\sim5°$ for the IGRF simulation) during $B_y^{IMF}+$ (sectors 0–3) in the NH.

[39] The scatter about the average direction within the 2 h bins (dotted lines) is more or less homogeneously distributed. The average ion drift directions across the central polar cap (not shown), on the other hand, show large scatter about a mean plasma motion close to the noon-midnight meridian ($\sim180°$) for northward IMF ($B_z^{IMF}+$) orientations. The B_y^{IMF} dependence of the ion drift directions is opposite to the B_y^{IMF} dependence of the neutral wind, i.e., the average

ion drift direction is slightly more dawnward in the NH for $B_y^{IMF}+$ and more dawnward in the SH for $B_y^{IMF}-$. This result may, however, not be very reliable due to the large scatter. It has to be analyzed in more detail in a dedicated future study.

[40] The average standard deviations of the neutral wind directions within $|\phi_m| > 80°$ magnetic latitude in Figure 12 (top) show a similar quasi-semidiurnal variation as the magnitudes shown in Figure 9 with the maxima for the SH slightly shifted to later hours: 10–12 UT and 20–22 UT, respectively. The time bin of maximum directional variation in the NH (12–14 UT) corresponds to that of the maximum magnitude variation; the second maximum appears to be time shifted to the 04–06 UT bin.

[41] The average standard deviations of the ion drift directions in Figure 12 (bottom) are also obviously different between the two model realizations. Almost coincident average standard deviations in the dipole case are contrasted by quasi-semidiurnal variations for the IGRF case with seemingly antiphase variation between the hemispheres. The
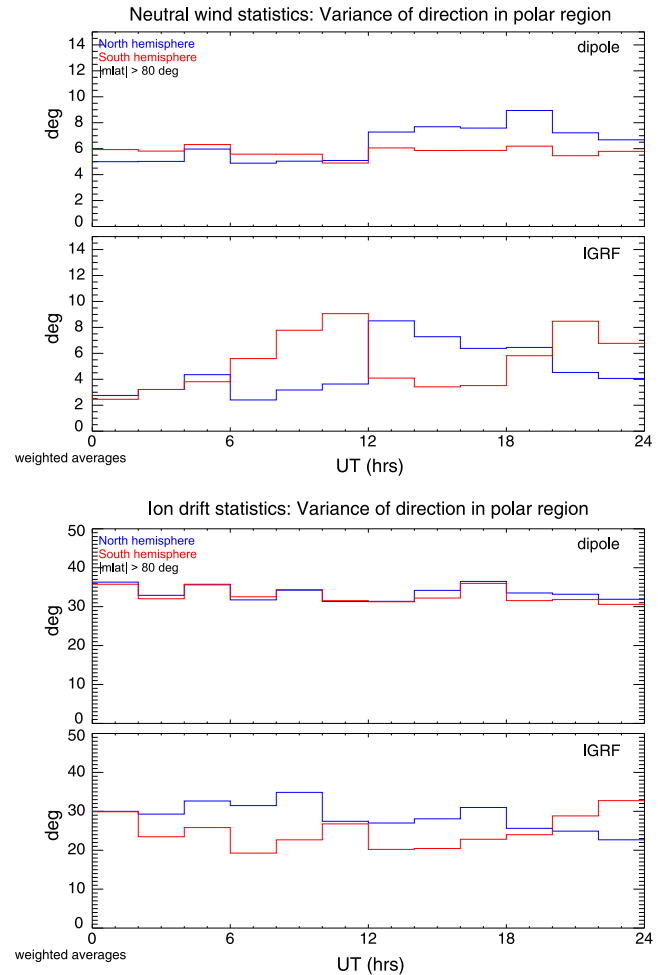

Figure 12. Diurnal variation of the standard deviations for the (top) modeled neutral wind (as shown in Figure 10) and (bottom) ion drift directions within the central polar cap regions ($|\phi_m| > 80°$). The blue and red lines stand for the NH and SH variations, respectively; each of the top and bottom panels for the two different model runs are similar to the other line plots above.
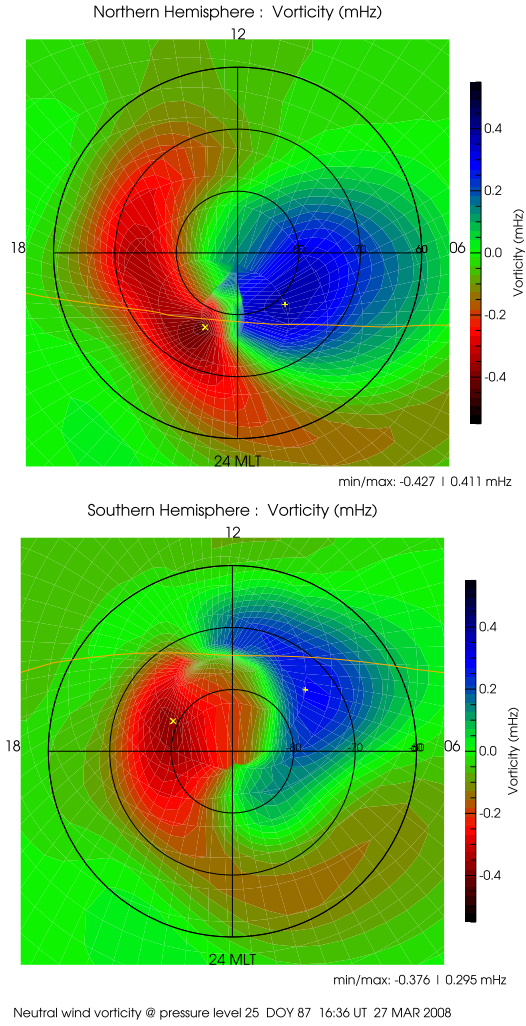
Figure 13. Neutral wind vorticity (radial component) at the polar regions of (top) the NH and (bottom) the SH in geomagnetic coordinates for the same IGRF model run and time as in Figure 3: 27 March 2008 at 16:36 UT. The minimum/maximum values are given on the bottom right of each plot and are indicated by a cross and a plus sign, respectively. The yellow line marks the terminator (solar zenith angle 90°).

diurnal variation clearly differs, however, from the neutral wind variation shown in Figure 12 (top).

3.3. Neutral Wind Vorticity and Divergence

[42] While accelerometer measurements allow the reconstruction of full horizontal wind vector patterns only within a circumpolar region and as condensed statistical averages [cf. *Förster et al.*, 2008], numerical simulation results can provide them globally at any instant. Such neutral wind vector patterns (and likewise also the ion drift plots) enable the derivation of further field characteristics like the vorticity $\omega_r = curl \; \vec{v}$ (radial component only) and divergence div $\vec{v} = \nabla_{hor} \cdot \vec{v}$ of the global horizontal neutral wind field as shown in Figures 13 and 14, respectively, for 16:36 UT of 27 March 2008.

[43] The vorticity of the horizontal wind field is calculated by applying Stoke's theorem to each bin. This is done similar to the study of *Sofko et al.* [1995] by integrating the flow along the closed path at each grid cell's boundary and dividing it by the bin's surface. The divergence is calculated correspondingly by summing up the flow across each grid cell's boundaries instead. These high-latitude distributions are shown here in Figures 13 and 14 for the same time as in Figure 3 as an example.

[44] The neutral wind vorticity is an indicator of the energy and momentum input from the solar wind drivers at high latitudes via the coupling with the ionized component. It dominates in particular at high latitudes over the divergence (both given in mHz) of the neutral wind field; please note the different scales for these parameters, given with the color bars on the right.

[45] The strongest divergence peak of positive values (upwelling) is seen in the northern high-latitude region at
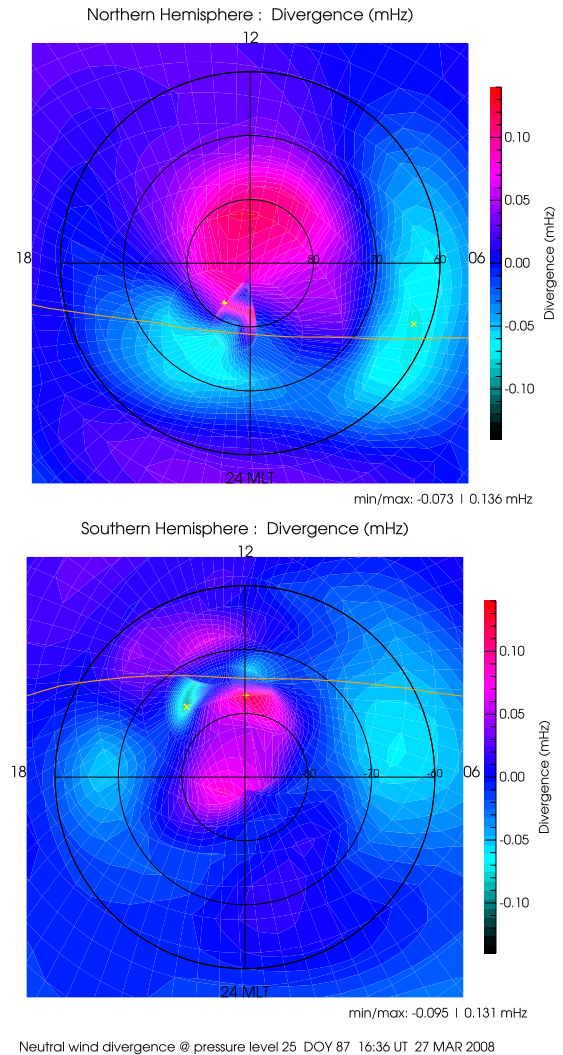

Figure 14. Neutral wind divergence in the polar regions of (top) the NH and (bottom) the SH in geomagnetic coordinates for the same IGRF model run and time as in Figure 3: 27 March 2008 at 16:36 UT. The minimum/maximum values are given on the bottom right of each plot. The yellow line marks the terminator (solar zenith angle 90°).
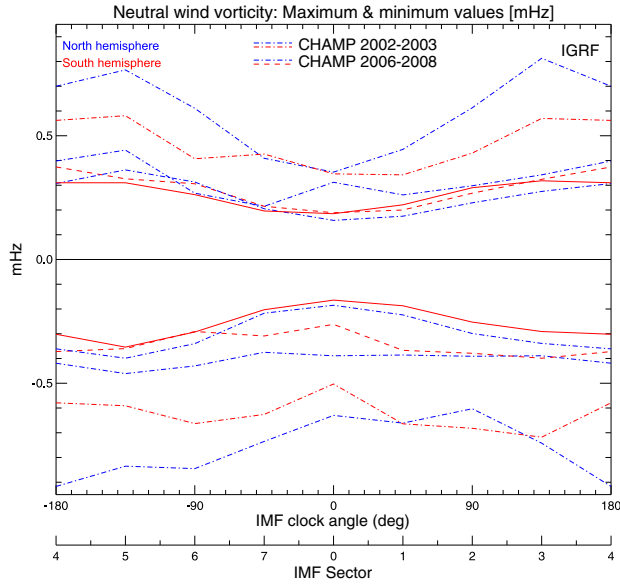
Figure 15. Neutral wind vorticity maximum and minimum values in the polar regions versus the IMF orientation (sectors). The IGRF model results (full lines, compare Table 1, lower part) for the NH (blue) and SH (red) are compared with corresponding results of two CHAMP data sets: from low solar activity in 2006–2008 (dashed lines, cf. Table 2, lower part) and from the high solar activity years 2002–2003 (dash-dotted lines, *Förster et al.* [2012, Table 1]).

slightly lower magnetic latitudes (∼78°, Figure 14, bottom). This divergence pattern is estimated with respect to a "breathing" atmosphere, to pressure level 25. The divergence signifies therefore a motion relative to or in addition to thermal expansion or contraction. It should be accompanied by small disturbances of the hydrostatic equilibrium [*Förster et al.*, 1999].

[46] The elongated ("crescent-shaped") red vortex with negative vorticity (clockwise (CW) circulation when viewed from above) between 60° and 80° northern geographic latitude (Figure 13, top) represents the well-known dusk cell of neutral air circulation in the northern polar region. In the SH (Figure 13, bottom), a large round dusk cell with a smaller peak value appears near 16 MLT (the cross within the red area: negative vorticity as for Figure 13, top, because viewed the same way from above the North Pole). The dawnside circulation cells of both hemispheres have at the same time an opposite polarity but smaller magnitudes than the dusk cells. The dawnside cell is round in the NH and more crescent-shaped in the SH. Such a pattern corresponds to $B_y^{\mathrm{IMF}}-$ and $B_z^{\mathrm{IMF}}-$ (sector 5) neutral wind circulations at high latitudes [cf. *Förster et al.*, 2011].

[47] To make some quantitative comparisons between the vorticity patterns in both hemispheres possible, Table 1 shows the minimum and maximum values for both model simulations, while Figure 15 illustrates the IGRF model results in comparison with averaged CHAMP observations from years of both high (2002–2003) and low (2006–2008) solar activity conditions. The model values were determined separately for each hemisphere after averaging the vorticity patterns of all 4800 instantaneous times. The model results agree better with the 2006–2008 CHAMP observations than with the 2002–2003 CHAMP observations—most likely because the solar activity levels are more similar.

local times near noon. This corresponds to 12 MLT and ∼82° magnetic latitude and indicates the cusp position (Figure 14, top). The cusp signature is much weaker at this particular time near noon in the SH and is located at

Table 1. Minimum and Maximum Values of High-Latitude Thermospheric Vorticity (mHz) in Both Hemispheres at Dusk and Dawn, Respectively, for All 4800 Data Points and Both the Dipole Case (Upper Part) and the IGRF Simulation (Lower Part), Sorted for the Eight Different IMF Clock Angle Sectors

IMF	North Hemisphere			South Hemisphere			Counts[a]	
Sector	Min	Max	Δ	Min	Max	Δ	#	%
Dipolar |B|-field model								
0	−0.183	0.156	0.339	−0.171	0.189	0.360	637	13.3
1	−0.221	0.175	0.396	−0.197	0.231	0.428	907	18.9
2	−0.297	0.229	0.527	−0.270	0.316	0.586	800	16.7
3	−0.338	0.273	0.611	−0.307	0.345	0.653	386	8.0
4	−0.359	0.303	0.662	−0.318	0.339	0.657	304	6.3
5	−0.396	0.354	0.749	−0.383	0.336	0.719	838	17.5
6	−0.334	0.309	0.642	−0.311	0.279	0.591	606	12.6
7	−0.216	0.201	0.417	−0.220	0.204	0.424	322	6.7
Average[b]	−0.291	0.247	0.539	−0.271	0.278	0.549	4800	100.
IGRF model simulation								
0	−0.185	0.158	0.343	−0.164	0.185	0.349	637	13.3
1	−0.224	0.175	0.399	−0.187	0.221	0.409	907	18.9
2	−0.299	0.229	0.528	−0.253	0.290	0.543	800	16.7
3	−0.339	0.275	0.614	−0.291	0.318	0.609	386	8.0
4	−0.361	0.307	0.668	−0.302	0.310	0.611	304	6.3
5	−0.399	0.362	0.761	−0.354	0.310	0.665	838	17.5
6	−0.340	0.313	0.653	−0.293	0.262	0.555	606	12.6
7	−0.217	0.205	0.422	−0.203	0.196	0.399	322	6.7
Average[b]	−0.294	0.250	0.545	−0.254	0.260	0.515	4800	100.

[a]The number of data points for each sector.
[b]The overall averages.

Table 2. Minimum and Maximum Values of High-Latitude Thermospheric Vorticity (mHz) as in Table 1 but Calculated Here From the Averaged Neutral Wind Pattern[a]

IMF	North Hemisphere			South Hemisphere			Counts	
Sector	Min	Max	Δ	Min	Max	Δ	#	%
	IGRF simulation: all data[a]						×10³	
0	−0.180	0.174	0.354	−0.196	0.186	0.382	308	13.3
1	−0.225	0.201	0.426	−0.207	0.191	0.398	439	18.9
2	−0.345	0.238	0.583	−0.297	0.268	0.565	388	16.7
3	−0.379	0.322	0.701	−0.384	0.230	0.684	187	8.0
4	−0.499	0.330	0.829	−0.316	0.465	0.781	147	6.3
5	−0.401	0.379	0.780	−0.312	0.378	0.690	406	17.5
6	−0.361	0.345	0.706	−0.269	0.319	0.588	293	12.6
7	−0.255	0.187	0.442	−0.187	0.286	0.473	155	6.7
Average	−0.264	0.235	0.499	−0.236	0.225	0.461	2323	100.
	IGRF simulation: Bias value ≥ 0.96[b]						×10³	
0	−0.180	0.181	0.361	−0.188	0.145	0.333	133	15.4
1	−0.242	0.159	0.401	−0.171	0.180	0.351	169	19.6
2	−0.449	0.239	0.688	−0.308	0.239	0.547	131	15.2
3	−0.391	0.398	0.789	−0.505	0.307	0.812	38	4.4
4	−0.598	0.382	0.980	−0.328	0.485	0.813	54	6.3
5	−0.431	0.408	0.839	−0.344	0.396	0.740	186	21.6
6	−0.344	0.357	0.701	−0.254	0.342	0.596	107	12.4
7	−0.214	0.296	0.510	−0.234	0.278	0.512	44	5.1
Average	−0.241	0.226	0.467	−0.238	0.214	0.452	862	100.
	CHAMP observations 2006–2008[c]						×10³	
0	−0.389	0.312	0.701	−0.262	0.189	0.451	739	8.5
1	−0.386	0.261	0.647	−0.367	0.200	0.567	1247	14.2
2	−0.391	0.298	0.689	−0.379	0.268	0.647	1554	17.8
3	−0.389	0.342	0.731	−0.399	0.324	0.723	1008	11.5
4	−0.419	0.398	0.817	−0.372	0.374	0.746	672	7.7
5	−0.461	0.442	0.903	−0.360	0.326	0.686	1036	11.8
6	−0.430	0.268	0.698	−0.291	0.306	0.596	1455	16.6
7	−0.375	0.215	0.590	−0.309	0.215	0.523	1038	11.9
Average	−0.388	0.267	0.655	−0.320	0.259	0.579	8748	100.

[a]The whole, unfiltered data.
[b]The corresponding bias-filtered (≥0.96) IGRF simulation data set.
[c]CHAMP observational results, averaged over the three full years 2006–2008 of low solar activity.

The difference (Δ) between the average maximum and minimum is also shown in Table 1. The last two columns provide the sector coverage during the 20 day model interval, which indicates a certain "leaning" of the IMF clock angle distribution from the usual maxima in sectors 2 and 6 toward sectors 1 and 5, respectively. This fact must be considered as an anomalous feature of this model interval which might have a certain influence on the results provided, in particular with regard to the clock angle dependencies (Figures 7 and 11).

[48] An interhemispheric comparison of the average vorticity maxima and minima in Table 1 shows that there are small differences in magnitude in favor of the NH for the IGRF model run, while these differences are negligible in the case of the dipole simulation. The average vorticity values have been calculated also for a "bias-value filtered" data set (with bias value of ≥0.96). This "bias-value filtering" of the IMF data is thought to select relatively stable IMF conditions for well-defined magnetospheric convection response patterns as a function of the eight discrete IMF clock angle sectors [cf. *Haaland et al.*, 2007]. The results obtained here for the average model vorticity values are, however, very similar to the values in Table 1 (not shown).

[49] The statistical vorticity pattern obtained from accelerometer measurements onboard satellites like CHAMP as shown in Figure 15 are determined in a somewhat different way. Rather than considering complete global vorticity patterns for each instantaneous model snapshot, satellite observations have to sample longer time intervals of neutral wind observations to obtain the complete circumpolar wind pattern (in the case of CHAMP these are ~131 days for full local time coverage, cf. *Förster et al.* [2008]). The vorticity values are then calculated from these averaged wind patterns [*Förster et al.*, 2011, 2012].

[50] We repeated, therefore, the averaging of vorticity values by emulating this procedure. The IMF sector-dependent means of the minimum and maximum high-latitude vorticity values in Table 2 are determined from the averaged global neutral horizontal wind pattern, sorted for the corresponding IMF sectors and, in case of the middle part of Table 2, filtered for certain IMF bias-value conditions. These results are compared with averaged CHAMP observations from the 3 years (2006–2008) of very low solar activity (bottom part of Table 2 and Figure 15).

[51] Comparing the values of Table 1 with those of Table 2 shows a good correspondence both between the different methods and between the model and observational results from the years of low solar activity. The dependence on IMF orientation (sectors) seems to be slightly more distinctive in Table 2 compared with the model averages of Table 1, which apparently yielded a larger smoothing of the minima and maxima. The NH vorticity values are slightly

larger than those in the SH, both for the IGRF simulation and the CHAMP observations (Table 1, lower part, and Table 2), while this difference almost vanishes for the dipole simulation (Table 1, upper part).

4. Discussion

[52] Our simulation results of the coupled magnetosphere-ionosphere-thermosphere (M-I-T) system, obtained by means of two different model approaches with and without symmetric geomagnetic conditions as explained in section 2.1, often show differences for the asymmetric (IGRF) case, when comparing the outcome parameters and their variations in the NH and SH (see section 3). This is already visible in the time series of the whole 20 day simulation interval (Figures 4, 5, and 8) but much clearer in the sortings of the data with respect to the UT variation (Figures 6, 9, 10, and 12) or IMF clock angle sectors (Figures 7 and 11). For all these comparisons, we selected data obtained within the narrow circumpolar regions with magnetic latitudes $|\phi_m| > 80°$, which represent the conditions within the central polar cap. Before using our model simulations to make inferences on the causes of observed differences in the NH and SH neutral winds and ion drifts, it makes sense to verify that the model is able to capture these variables reasonably well in the high-latitude upper thermosphere. We therefore first offer some comparisons with observations of these variables.

[53] The largest magnitudes of neutral wind speed anywhere on the globe have been observed within the high-latitude upper thermosphere. Long-term observations with ground-based Fabry-Perot interferometers (FPI) located at Thule and Søndre Strømfjord, Greenland, for example, showed typical wind speeds of about 200 m/s at solar minimum, rising up to about 800 m/s at solar maximum, depending on the geomagnetic activity level [*Killeen et al.*, 1995]. Our model simulation results (Figure 4) show an average level of neutral thermospheric wind velocities across the central polar cap region of about 300 m/s. Peak values of up to 800 m/s are obtained, and the corresponding plasma drift velocities rise up to 1600 m/s as shown in Figure 5. These extreme values occur during the moderate geomagnetic storm periods on DoY 86 (26 March) and 95 (4 April).

[54] An empirical climatology of the quiet-time ($Kp < 3$) upper thermospheric neutral wind for a broad range of solar activity conditions measured by seven ground-based Fabry-Perot Interferometers (FPIs) was provided by *Emmert et al.* [2006a, 2006b]. Their comprehensive compilation of neutral wind observations for both hemispheres suggests average nightside near-polar wind speeds for moderate solar activity ($F_{10.7}$ = 140) during geomagnetically quiet times of the order of 150–200 m/s [*Emmert et al.*, 2006a, Figure 5]. These average values concern the two stations closest to the pole, namely, Søndre Strømfjord (magnetic QD latitude 73.3°N) and South Pole (74.2°S). In comparison to CHAMP accelerometer measurements at high magnetic latitudes [*Förster et al.*, 2008, 2011] and to our model results, these wind magnitudes are smaller by about a factor of 2. This discrepancy could be explained by the presence of storm time periods during the model interval. According to the results of *Emmert et al.* [2008], which describe storm

time winds, another 100–150 m/s average wind speed could be added to the quiet-time polar cap winds at 250 km.

[55] FPI measurements are, however, essentially taken from a lower altitude ($\sim$ 250 km), integrating usually over a larger altitude range. The CHAMP satellite measurements as well as effectively the model results, on the other hand, represent in situ observations near 400 km height; i.e., they stand for upper thermosphere conditions, where direct measurements are rare. In situ thermospheric wind measurements were obtained in the 1970s and early 1980s by the AE-C and DE 2 satellites. Their published measured wind magnitudes are comparable with the magnitudes obtained in this study [e.g., *Hays et al.*, 1984; *Killeen et al.*, 1995].

[56] The overall mean of the modeled ion drift magnitude values in the central polar caps for the IGRF case (cf. Figure 5) are 386 m/s and 320 m/s in the NH and SH, respectively (the median values are 370 m/s and 357 m/s accordingly); the average standard deviation values are about 135 m/s for both hemispheres. This corresponds quite well to average values of EDI/Cluster estimates of total averages for 2003 with 576 m/s and 520 m/s in the NH and SH, respectively, according to Tables 1 and 2 of *Förster et al.* [2008]. The magnitudes themselves do not match, considering the difference in solar and geomagnetic activity conditions during 2003 versus the model interval in 2008, but the hemispheric difference is in the right sense and so is consistent with the model results.

[57] Cross-polar cap ion drift velocities are usually measured and compared as CPCP values, i.e., the difference between maximum and minimum values of the electric potential (Φ) distribution over the polar cap. This is related to the ion drift velocities via the local magnetic flux density $\vec{B}$ according to $\vec{v} \times \vec{B}$ = grad Φ. The EDI/Cluster electric potential patterns and their dependence on the IMF have been shown to correspond well to other satellite estimates and ground-based observations like those of the Super-DARN network for both hemispheres as shown, e.g., by *Haaland et al.* [2007, Figure 9] and *Cousins and Shepherd* [2010, Figure 8]. CMIT does tend to overestimate the CPCP during disturbance intervals, and as a result the high-latitude ion drifts, and to a lesser extent the neutral winds, may be too strong as well. The paper by *Wiltberger et al.* [2012] cited in section 2.2 has found that this is also the case for the interval we studied.

[58] The comparison of vorticity estimates from CHAMP observations of the years 2002–2003 [*Förster et al.*, 2012, Table 1] with those of the IGRF simulation in Tables 1 and 2 as well as with the CHAMP observations from 2006–2008 (Table 2, bottom part, and Figure 15) show that both the average maximum and minimum vorticity values during the model interval (lowest solar activity) seems to be about half as large in magnitude as observed. Other observational studies covering multiple solar cycles indicate that high-latitude wind speeds increase with increasing solar activity [e.g., *Emmert et al.*, 2006a, 2006b]. Since vorticity and wind speed should be strongly and positively related, the observed decrease in vorticity from 2002–2003 to 2006–2008 is likely due to the corresponding decrease in solar activity between these intervals. The 2008 CMIT model vorticity magnitudes are partly smaller than the observed ones from 2006 to 2008, in particular for the dawnside minimum values for northward and duskward

IMF (sectors 7 and 0–3). This difference between measured and modeled vorticity values is likely due in part to solar activity; however, a bias in the model simulation could also be contributing.

[59] The observed north-south differences for both the minimum and maximum vorticity in this model interval of less than 10% are in obvious contrast to the ~30% difference for CHAMP 2002/2003 [*Förster et al.*, 2011, 2012]. Given the relationship between the vorticity magnitudes and solar activity, it is reasonable to assume that the NH-SH vorticity differences are also affected by solar activity. The small interhemispheric vorticity differences in the 2008 CMIT simulation are consistent with the observational results of 2006–2008, suggesting that small NH-SH vorticity differences are associated with solar minimum conditions.

[60] In contrast to our results, *Thayer and Killeen* [1993] found stronger neutral winds in the SH polar cap than in the NH polar cap. This apparent contradiction is likely due to the different seasons being analyzed. *Thayer and Killeen* [1993] studied December solstice conditions (summer in the SH) rather than the equinox conditions that are considered here. The larger plasma densities in the summer polar region that are associated with continuous solar illumination are expected to result in a stronger coupling between the ions and neutrals, which could lead to a stronger forcing of the neutrals at high latitudes, in particular when contrasted with winter conditions. Perhaps this could overcome the influence of the magnetic field asymmetry, which acts in the opposite direction. However, further analysis needs to be done to investigate such seasonal effects further and confirm this, which is beyond the scope of this study.

[61] Comparing the two model runs, it is clear that using the IGRF simulation leads to larger hemispheric differences. We conclude that the asymmetry of the Earth's magnetic field does seem to contribute to the observed hemispheric differences. But how much can it explain and which way is it realized within the complex coupled M-I-T system? And are the differences likely to be due to differences in magnetic flux densities $|\vec{B}|$ at high latitudes in the opposite hemispheres? Or are they rather due to the different offsets of the invariant magnetic poles?

[62] The magnetic field at magnetic latitudes $|\phi_m| > 80°$ is on average weaker in the NH than in the SH (Figure 1). A weaker magnetic field should lead to stronger high-latitude $\vec{E} \times \vec{B}$ drifts and neutral winds [*Cnossen et al.*, 2011]. This is consistent with observations of, e.g., the EDI/Cluster instrument as presented by *Förster et al.* [2007]. There it was shown that the average ionospheric drift magnitude is about 7% larger at high latitudes of the NH compared with the SH. Likewise, the cross-polar neutral wind magnitudes according to CHAMP data are on average larger over the NH than over the SH [*Förster et al.*, 2008, 2011]. The hemispheric difference in magnetic field strength could thus explain why we find consistently larger plasma drifts and neutral winds in the NH. However, the asymmetry in magnetic field structure probably contributes as well. The invariant magnetic pole has a smaller offset from the rotation axis in the NH than in the SH, which could be interpreted as a smaller tilt angle. *Cnossen and Richmond* [2012] showed that a smaller tilt angle gives a larger CPCP and more Joule heating, causing both high-latitude $\vec{E} \times \vec{B}$ drifts and neutral winds to be stronger on average. This effect was most important

during southward IMF conditions (sector 4). This matches very well with our findings here, which show the strongest hemispheric differences in plasma drift and neutral wind for southward IMF (see Figure 7).

[63] Neutral winds are driven by collisions with ions as well as by neutral temperature gradients, caused by spatial differences in solar illumination and Joule heating. Solar illumination causes temperature gradients mainly in the north-south direction of a geographic reference frame, whereas Joule heating creates temperature gradients mainly in the north-south direction of a geomagnetic reference frame and predominantly at high latitudes. The Coriolis force is likewise organized in the geographic frame, while the electromagnetic forces via ion-neutral drag are bound to geomagnetic coordinates. A larger offset between the geographic and invariant magnetic poles might therefore be expected to result in a more complex neutral wind pattern with greater spatial variability. This predicts greater spatial variation in plasma drifts and neutral winds in the SH, which is indeed what we find (Figure 8).

[64] A larger offset between the geographic and invariant magnetic poles (i.e., larger tilt angle) is also expected to lead to greater variation over the course of a day. *Cnossen et al.* [2012b] showed that the cross-polar cap potential minimizes when the polar cap is tilted maximally towards or away from the Sun (during equinox at 04:40 UT and 16:40 UT for a dipole position at 70°W) and maximizes in between (at 10:40 UT and 22:40 UT for the same conditions). The semidiurnal minima are deeper for a larger dipole tilt, with maxima being roughly the same for different dipole tilts [*Cnossen and Richmond*, 2012]. A larger cross-polar cap potential is usually linked to stronger $\vec{E} \times \vec{B}$ drifts and neutral winds. Any differences between the NH and SH plasma drift and neutral wind that are related to differences in geographic and invariant magnetic pole offset might therefore be expected to be most prominent near 04:40 and 16:40 UT. The semidiurnal variation of the north-south difference, as shown in Figure 6, lets us suppose a slight tendency in this direction, given the maximum distances between NH and SH for the IGRF case in the UT ranges between ~04–10 UT and 16–22 UT.

5. Conclusions

[65] We have performed two different model simulations of the coupled M-I-T system for a 20 day interval near spring equinox of 2008 to study the effects of different magnetic flux densities $|\vec{B}|$ and different offsets of the invariant magnetic poles from the geographic ones in the opposite hemispheres, as they are observed for the present-day magnetosphere. In the first run with the CMIT model we assumed a symmetrically tilted dipolar geomagnetic system, while in a second model run we assumed the IGRF magnetic field configuration for the simulation of the globally coupled system. The modeling results show substantial differences in the average ionospheric drift and neutral wind parameters at high magnetic latitudes of the opposite hemispheres within the central polar caps for the IGRF case, while the dipole simulation resulted mostly in symmetrically coincident parameter variations.

[66] The IGRF simulation results suggest 10–15% larger cross-polar neutral wind magnitudes in the NH compared

with the SH in case of the more realistic magnetic field configurations. The high-latitude ionospheric plasma drift at *F* region heights shows likewise a difference of the average magnitudes in favor of the NH. This hemispheric difference for both parameters could be due to distinct differences of magnetic flux densities in the opposite near-polar regions and to a certain degree also due to the north-south difference in offsets between the invariant magnetic and the geographic poles.

[67] On the other hand, the average spatial variance of the neutral wind magnitude for the IGRF model run only is larger within the central polar cap in the SH compared with the NH for most local times, showing a pronounced diurnal variation. Maximum differences are seen in the 06–12 UT range, and a secondary maximum starts with the 18–20 UT bin and lasts until ∼00 UT. The variances of directional averages at high latitudes of the SH prevail similarly in the diurnal variation but with an intermittent dominance of the NH variances for the period 12–18 UT. The larger variance in the SH is most likely associated with the larger offset between the geographic pole and the invariant magnetic pole in the SH, although we do not fully understand the UT dependence.

[68] The variation of the average cross-polar ion drift and neutral wind circulation shows the familiar B_z^{IMF} dependence in magnitude for both model realizations, with small values for northward IMF and steadily increasing values for southward turning. An offset between the ion drift magnitudes and the wind magnitudes appears for all IMF clock angles only in case of the IGRF model run. The modulation of the neutral thermospheric wind magnitude with the B_y^{IMF} component is seen in both model simulations, with larger values in the NH for $B_y^{IMF}-$ (sector ∼5) compared with $B_y^{IMF}+$ conditions (sector ∼3) and the opposite tendency for the SH. The fact that both simulations show a similar modulation indicates that it is not caused or amplified by the asymmetry of the magnetic field. The relative offsets of the interhemispheric differences seem to be stronger for $B_y^{IMF}-$ conditions. These variations with the IMF orientation could also be noticed in observational data of the CHAMP accelerometer measurements and in EDI/Cluster average ion drift patterns. The directly antisolar cross-polar cap drift for $B_z^{IMF}-$ and $B_y^{IMF}-$ conditions (sector 5) in the NH favors the cross-polar neutral wind circulation, while $B_z^{IMF}-$ and $B_y^{IMF}+$ conditions cause a duskward deflection by means of ion drag. Correspondingly, in the SH the conditions are mirrored with respect to the B_y^{IMF} sign.

[69] Certain characteristics of the neutral winds and ion drifts show similar north-south differences (e.g., the magnitudes of both winds and drifts are larger in the NH compared with the SH in the IGRF case, cf. Figures 6 and 7), while other characteristics, like the UT dependence of the variance of the neutral wind and ion drift directions (Figure 12), show different hemispheric differences of the neutral and ionized constituents. The differences between the opposite hemispheres are most likely due to the different offsets of the invariant magnetic poles. The neutrals respond to electromagnetic forces and Joule heating on the one hand, which are coupled to geomagnetic coordinates, and to forcings like thermal heating from the dayside on the other hand, which are bound to a geographic reference frame. Due to the close coupling between the neutral and the ionized component in

the upper atmosphere (∼400 km), together with the greater difference in the alignment of geomagnetic and geographic forces in the SH, the spatial variance of the neutral wind in the SH is generally larger and more strongly UT dependent.

[70] Further information on the influence of the asymmetry of the magnetic field on the upper atmosphere could be gained by additional observational evidence, e.g., from near-Earth satellite missions like CHAMP and the forthcoming Swarm ionospheric multisatellite project [*Friis-Christensen et al.*, 2006, 2009]. Future investigations on hemispheric differences of the high-latitude energy and momentum input should identify the observable parameters and environmental conditions, which would help to clarify the role of magnetic field asymmetry. It will be of interest, in particular, how and to what extent different aspects of the magnetic field asymmetry (offset, magnitude, and pattern structure) contribute to different aspects of hemispheric differences in the neutral and ionized parameters in the high-latitude upper atmosphere. Follow-up studies will also have to clarify possible distinctions with respect to the September equinox behavior and address hemispheric asymmetries under solstice conditions, in order to understand differences between NH and SH winter and between NH and SH summer.

References

A, E., A. J. Ridley, D. Zhang, and Z. Xiao (2012), Analyzing the hemispheric asymmetry in the thermospheric density response to geomagnetic storms, *J. Geophys. Res.*, *117*, A08317, doi:10.1029/2011JA017259.

Baker, K. B., and S. Wing (1989), A new magnetic coordinate system for conjugate studies at high latitudes, *J. Geophys. Res.*, *94*(A7), 9139–9143.

Bisi, M. M., B. J. Thompson, B. A. Emery, S. E. Gibson, J. Leibacher, and L. van Driel-Gesztelyi (2011), The Sun–Earth connection near solar minimum: Placing it into context, *Sol. Phys.*, *274*(1–2), 1–3.

Cnossen, I., and A. D. Richmond (2012), How changes in the tilt angle of the geomagnetic dipole affect the coupled magnetosphere-ionosphere-thermosphere system, *J. Geophys. Res.*, *117*, A10317, doi:10.1029/2012JA018056.

Cnossen, I., A. D. Richmond, M. Wiltberger, W. Wang, and P. Schmitt (2011), The response of the coupled magnetosphere-ionosphere-thermosphere system to a 25% reduction in the dipole moment of the Earth's magnetic field, *J. Geophys. Res.*, *116*, A12304, doi:10.1029/2011JA017063.

Cnossen, I., A. D. Richmond, and M. Wiltberger (2012a), The dependence of the coupled magnetosphere-ionosphere-thermosphere system on the Earth's magnetic dipole moment, *J. Geophys. Res.*, *117*, A05302, doi:10.1029/2012JA017555.

Cnossen, I., M. Wiltberger, and J. E. Ouellette (2012b), The effects of seasonal and diurnal variations in the Earth's magnetic dipole orientation on solar wind-magnetosphere-ionosphere coupling, *J. Geophys. Res.*, *117*, A11211, doi:10.1029/2012JA017825.

Constable, C., and M. Korte (2006), Is Earth's magnetic field reversing?, *Earth Planet. Sci. Lett.*, *246*(1–2), 1–16.

Cousins, E. D. P., and S. G. Shepherd (2010), A dynamical model of high-latitude convection derived from SuperDARN plasma drift measurements, *J. Geophys. Res.*, *115*, A12329, doi:10.1029/2010JA016017.

Doornbos, E., J. van den IJssel, H. Lühr, M. Förster, and G. Koppenwallner (2010), Neutral density and crosswind determination from arbitrarily oriented multi-axis accelerometers on satellites, *J. Spacecraft and Rockets*, *47*(4), 580–589, doi:10.2514/1.48114.

Emmert, J. T., M. L. Faivre, G. Hernandez, M. J. Jarvis, J. W. Meriwether, R. J. Niciejewski, D. P. Sipler, and C. A. Tepley (2006a), Climatologies of nighttime upper thermospheric winds measured by ground-based Fabry-Perot interferometers during geomagnetically quiet conditions: 1. Local

FÖRSTER AND CNOSSEN: NORTH-SOUTH DIFFERENCES OF M-I-T SYSTEM

time, latitudinal, seasonal, and solar cycle dependence, *J. Geophys. Res.*, *111*, A12302, doi:10.1029/2006JA011948.

Emmert, J. T., G. Hernandez, M. J. Jarvis, R. J. Niciejewski, D. P. Sipler, and S. Vennerstrom (2006b), Climatologies of nighttime upper thermospheric winds measured by ground-based Fabry-Perot interferometers during geomagnetically quiet conditions: 2. High-latitude circulation and interplanetary magnetic field dependence, *J. Geophys. Res.*, *111*, A12303, doi:10.1029/2006JA011949.

Emmert, J. T., D. P. Drob, G. G. Shepherd, G. Hernandez, M. J. Jarvis, J. W. Meriwether, R. J. Niciejewski, D. P. Sipler, and C. A. Tepley (2008), DWM07 global empirical model of upper thermospheric storm-induced disturbance winds, *J. Geophys. Res.*, *113*, A11319, doi:10.1029/2008JA013541.

Emmert, J. T., A. D. Richmond, and D. P. Drob (2010), A computationally compact representation of Magnetic-Apex and Quasi-Dipole coordinates with smooth base vectors, *J. Geophys. Res.*, *115*, A08322, doi:10.1029/2010JA015326.

Escoubet, C. P., R. Schmidt, and M. L. Goldstein (1997), Cluster—Science and mission overview, *Space Sci. Rev.*, *79*, 11–32.

Finlay, C. C., et al. (2010), International Geomagnetic Reference Field: The eleventh generation, *Geophys. J. Int.*, *183*(3), 1216–1230, doi:10.1111/j.1365-246X.2010.04804.x.

Förster, M., A. A. Namgaladze, and R. Y. Yurik (1999), Thermospheric composition changes deduced from geomagnetic storm modeling, *Geophys. Res. Lett.*, *26*, 2625–2628.

Förster, M., G. Paschmann, S. E. Haaland, J. M. Quinn, R. B. Torbert, C. E. McIlwain, H. Vaith, P. A. Puhl-Quinn, and C. A. Kletzing (2007), High-latitude plasma convection from Cluster EDI: Variances and solar wind correlations, *Ann. Geophys.*, *25*(7), 1691–1707.

Förster, M., S. Rentz, W. Köhler, H. Liu, and S. E. Haaland (2008), IMF dependence of high-latitude thermospheric wind pattern derived from CHAMP cross-track measurements, *Ann. Geophys.*, *26*(6), 1581–1595.

Förster, M., Y. I. Feldstein, S. E. Haaland, L. A. Dremukhina, L. I. Gromova, and A. E. Levitin (2009), Magnetospheric convection from Cluster EDI measurements compared with the ground-based ionospheric convection model IZMEM, *Ann. Geophys.*, *27*(8), 3077–3087.

Förster, M., S. E. Haaland, and E. Doornbos (2011), Thermospheric vorticity at high geomagnetic latitudes from CHAMP data and its IMF dependence, *Ann. Geophys.*, *29*(1), 181–186.

Förster, M., B. E. Prokhorov, A. A. Namgaladze, and M. Holschneider (2012), Numerical modeling of solar wind influences on the dynamics of the high-latitude upper atmosphere, *Adv. Radio Sci.*, *10*, 299–312.

Friis-Christensen, E., H. Lühr, and G. Hulot (2006), Swarm: A constellation to study the Earth's magnetic field, *Earth Planets Space*, *58*(A2), 351–358.

Friis-Christensen, E., H. Lühr, D. Knudsen, and R. Haagmans (2009), Swarm—An Earth Observation Mission investigating Geospace, *Adv. Space Res.*, *41*(1), 210–216.

Haaland, S. E., G. Paschmann, and B. U. Ö. Sonnerup (2006), Comment on "A new interpretation of Weimer et al.'s solar wind propagation delay technique" by Bargatze et al, *J. Geophys. Res.*, *111*, A06102, doi:10.1029/2005JA011376.

Haaland, S. E., G. Paschmann, M. Förster, J. M. Quinn, R. B. Torbert, C. E. McIlwain, H. Vaith, P. A. Puhl-Quinn, and C. A. Kletzing (2007), High-latitude plasma convection from Cluster EDI measurements: Method and IMF-dependence, *Ann. Geophys.*, *25*(1), 239–253.

Hagan, M. E., and J. M. Forbes (2002), Migrating and nonmigrating diurnal tides in the middle and upper atmosphere excited by tropospheric latent heat release, *J. Geophys. Res.*, *107*(D24), 4754, doi:10.1029/2001JD001236.

Hagan, M. E., and J. M. Forbes (2003), Migrating and nonmigrating semidiurnal tides in the middle and upper atmosphere excited by tropospheric latent heat release, *J. Geophys. Res.*, *108*(A2), 1062, doi:10.1029/2002JA009466.

Hays, P. B., T. L. Killeen, N. W. Spencer, L. E. Wharton, R. G. Roble, B. A. Emery, T. J. Fuller-Rowell, D. Rees, L. A. Frank, and J. D. Craven (1984), Observations of the dynamics of the polar thermosphere, *J. Geophys. Res.*, *89*(A5), 5597–5612.

Hultqvist, B (1958), The geomagnetic field lines in higher approximations, *Ark. Geofys.*, *3*, 63–77.

Killeen, T. L., Y.-I. Won, R. J. Niciejewski, and A. G. Burns (1995), Upper thermosphere winds and temperatures in the geomagnetic polar cap: Solar cycle, geomagnetic activity, and interplanetary magnetic field dependencies, *J. Geophys. Res.*, *100*(A11), 21,327–21,342.

Korte, M., and M. Mandea (2008), Magnetic poles and dipole tilt variation over the past decades to millennia, *Earth Planets Space*, *60*(9), 937–948.

Lyon, J. G., J. A. Fedder, and C. M. Mobarry (2004), The Lyon-Fedder-Mobarry (LFM) global MHD magnetospheric simulation code, *J. Atmos. Sol. Terr. Phys.*, *66*(15-16), 1333–1350, doi:10.1016/j.jastp.2004.04.020.

Merkin, V. G., and J. G. Lyon (2010), Effects of the low-latitude ionospheric boundary condition on the global magnetosphere, *J. Geophys. Res.*, *115*, A10202, doi:10.1029/2010JA015461.

Olsen, N., and M. Mandea (2007), Will the magnetic north pole move to Siberia?, *Eos Trans. AGU*, *88*(29), 293–293.

Papitashvili, V. O., and F. J. Rich (2002), High-latitude ionospheric convection models derived from Defense Meteorological Satellite Program ion drift observations and parameterized by the interplanetary magnetic field strength and direction, *J. Geophys. Res.*, *107*(A8), 1198, doi:10.1029/2001JA000264.

Paschmann, G., et al. (1997), The electron drift instrument for cluster, *Space Sci. Rev.*, *79*(1–2), 233–269.

Paschmann, G., et al. (2001), The electron drift instrument on cluster: Overview of first results, *Ann. Geophys.*, *19*, 1273–1288.

Reigber, C., H. Lühr, and P. Schwintzer (2002), CHAMP mission status, *Adv. Space Res.*, *30*, 129–134.

Richmond, A. D. (1995), Ionospheric electrodynamics using magnetic Apex coordinates, *J. Geomag. Geoelectr.*, *47*, 191–208.

Richmond, A. D., E. C. Ridley, and R. G. Roble (1992), A thermosphere/ionosphere general circulation model with coupled electrodynamics, *Geophys. Res. Lett.*, *19*(6), 601–604.

Roble, R. G., E. C. Ridley, A. D. Richmond, and R. E. Dickinson (1988), A coupled thermosphere/ionosphere general circulation model, *Geophys. Res. Lett.*, *15*, 1325–1328.

Ruohoniemi, J. M., and R. A. Greenwald (2005), Dependencies of high-latitude plasma convection: Consideration of interplanetary magnetic field, seasonal, and universal time factors in statistical patterns, *J. Geophys. Res.*, *110*, A09204, doi:10.1029/2004JA010815.

Sofko, G. J., R. A. Greenwald, and W. A. Bristow (1995), Direct determination of large-scale magnetospheric field-aligned currents with Super-DARN, *Geophys. Res. Lett.*, *22*(15), 2041–2044.

Thayer, J. P., and T. L. Killeen (1993), A kinematic analysis of the high-latitude thermospheric neutral circulation pattern, *J. Geophys. Res.*, *98*(A7), 11,549–11,565.

Wang, W., M. Wiltberger, A. G. Burns, S. C. Solomon, T. L. Killeen, N. Maruyama, and J. G. Lyon (2004), Initial results from the coupled magnetosphere-ionosphere-thermosphere model: Thermosphere-ionosphere responses, *J. Atmos. Sol. Terr. Phys.*, *66*(15-16), 1425–1441, doi:10.1016/j.jastp.2004.04.008.

Wang, W., J. Lei, A. G. Burns, M. Wiltberger, A. D. Richmond, S. C. Solomon, T. L. Killeen, E. R. Talaat, and D. N. Anderson (2008), Ionospheric electric field variations during a geomagnetic storm simulated by a coupled magnetosphere ionosphere thermosphere (CMIT) model, *Geophys. Res. Lett.*, *35*, L18105, doi:10.1029/2008GL035155.

Weimer, D. R., D. M. Ober, N. C. Maynard, M. R. Collier, D. J. McComas, N. F. Ness, C. W. Smith, and J. Watermann (2003), Predicting interplanetary magnetic field (IMF) propagation delay times using the minimum variance technique, *J. Geophys. Res.*, *108*(A1), 1026, doi:10.1029/2002JA009405.

Wiltberger, M., W. Wang, A. G. Burns, S. C. Solomon, J. G. Lyon, and C. C. Goodrich (2004), Initial results from the coupled magnetosphere-ionosphere-thermosphere model: Magnetospheric and ionospheric responses, *J. Atmos. Sol. Terr. Phys.*, *66*(15-16), 1411–1423, doi:10.1016/j.jastp.2004.04.026.

Wiltberger, M., R. S. Weigel, W. Lotko, and J. A. Fedder (2009), Modeling seasonal variations of auroral particle precipitation in a global-scale magnetosphere-ionosphere simulation, *J. Geophys. Res.*, *114*, A01204, doi:10.1029/2008JA013108.

Wiltberger, M., L. Qian, C.-L. Huang, W. Wang, R. E. Lopez, A. G. Burns, S. C. Solomon, Y. Deng, and Y. Huang (2012), CMIT study of CR2060 and 2068 comparing L1 and MAS solar wind drivers, *J. Atmos. Sol. Terr. Phys.*, *83*, 39–50, doi:10.1016/j.jastp.2012.01.005.